Research Article | **Open Access**

Soft Science

Wang *et al*. *Soft Sci*. **2026**, *6*, 44 **DOI:**10.20517/ss.2026.27

Bioinspired structural coupling of superhydrophobicity and sensing for ternary interactions

Yu Wang[1,#], **Yimeng Xu**[1,#], **Ziyi Dai**[1,2,#,*], **Mingrui Wang**[3], **Wenbin Xu**[4,*], **Qingmeng Zhang**[5,*], **Yizhi Liu**[6,*], **Kai Qian**[1,*]

Keywords: Soft robotics, bionics, crack sensor, superhydrophobicity, ternary interaction system

Citation: Wang, Y.; Xu, Y.; Dai, Z.; Wang, M.; Xu, W.; Zhang, Q.; Liu, Y.; Qian, K. Bioinspired structural coupling of superhydrophobicity and sensing for ternary interactions. *Soft Sci.* **2026**, *6*, 44. https://dx.doi.org/10.20517/ss.2026.27

Received: 4 Feb 2026
First Decision: 19 Mar 2026
Revised: 1 Apr 2026
Accepted: 27 Apr 2026
Published: 1 Jun 2026

Academic Editors: Kuniharu Takei, Carlo Massaroni
Copy Editor: Shu-Yuan Duan
Production Editor: Shu-Yuan Duan

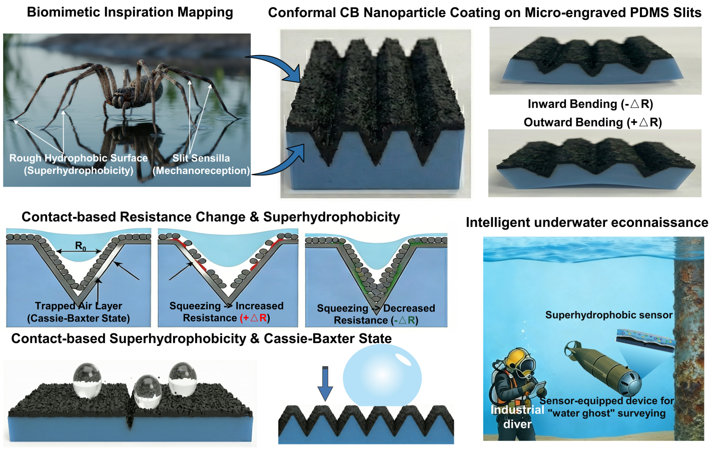

Abstract

Developing amphibious human-machine interfaces (HMIs) with high information density is pivotal for the next generation of soft robotics and Internet of Things. However, current resistive sensors face a fundamental tradeoff wherein the extrinsic encapsulation required for waterproofing inevitably restricts the formation of microstructures essential for high-sensitivity contact sensing, thereby suppressing the directional discriminability required for advanced logic. Herein, we report a monolithic superhydrophobic sensor that resolves this conflict through a facile mechanical microengraving and solvent-assisted swelling strategy. This system is inspired by the structural monism of the semiaquatic fishing spider. Distinct from conventional coating methods that introduce parasitic insulating layers, our approach embeds conductive carbon black nanoparticles directly into

---

[1]School of Integrated Circuits, Shandong University, Jinan 250100, China.
[2]Shenzhen Research Institute of Shandong University, Shenzhen, 518000, China.
[3]Department of Mechanical Engineering, University of Auckland, Auckland 1010, New Zealand.
[4]International Joint Institute of Tianjin University, Fuzhou, 350205, China.
[5]Department of Orthopaedics, Qilu Hospital of Shandong University, Jinan, 250100, China.
[6]Department of Astronautical Science and Mechanics, Harbin Institute of Technology, Harbin, 150001, China.
[#]These authors contributed equally to this work.

[*]**Correspondence to:** Dr. Ziyi Dai, School of Integrated Circuits, Shandong University, Jinan, 250100, China. Shenzhen Research Institute of Shandong University, Shenzhen 518000, Guangdong, China. E-mail: ziyidai@sdu.edu.cn; Prof. Wenbin Xu, International Joint Institute of Tianjin University, Fuzhou 350205, Fujian, China. E-mail: xuwb@aircas.ac.cn; Dr. Qingmeng Zhang, Department of Orthopaedics, Qilu Hospital of Shandong University, Jinan 250100, Shandong, China. E-mail: zhangqingmeng@email.sdu.edu.cn; Prof. Yizhi Liu, Department of Astronautical Science and Mechanics, Harbin Institute of Technology, Harbin 150001, Heilongjiang, China. E-mail: liuyizhi@hit.edu.cn;

Prof. Kai Qian, School of Integrated Circuits, Shandong University, Jinan 250100, Shandong, China. E-mail: kaiqian@sdu.edu.cn

the polymer matrix. This creates an "interface-free" architecture that sustains a robust air plastron for intrinsic superhydrophobicity (contact angle of > 153°) while preserving direct electromechanical contact. Consequently, the sensor exhibits exceptional environmental immunity against corrosive fluids (acid, alkali, and saline solutions) and achieves high-fidelity bidirectional mechanotransduction, capable of decoupling the bidirectional bending with a rapid response (rise and recovery times of 240 and 200 ms, respectively). Leveraging these unique properties, we demonstrate a ternary-logic interaction system that exponentially expands the command capacity of wearable HMI devices. Moreover, a "aquatic phantom" robotic skin that can acquire actionable spatial information through directional collision perception in underwater environments is demonstrated. This work establishes a generic design paradigm for engineering environment-adaptive, intelligent skins that function reliably across the terrestrial-aquatic boundary.

INTRODUCTION

The rapid evolution of the Internet of Things and soft robotics is catalyzing a paradigm shift in human-machine interaction (HMI) from simple binary controls to high-dimensional, intelligent feedback systems[1-9]. Traditional wearable interfaces primarily function as binary switches where the output toggles between an idle state "0" and an active state "1" regardless of the stimulus direction, which inherently restricts the information density of individual devices[10,11]. To support the sophisticated control requirements of emerging humanoid robots while maintaining minimalist hardware architectures, there is an urgent need for resistive sensors possessing directional self-decoupling capabilities; in particular, the ability to encode diverse mechanical stimuli into distinguishable ternary signals is required[12,13]. In this context, the states "-1," "0," and "1" qualitatively represent inward bending (negative phase), idle, and outward bending (positive phase) deformation modes, respectively, rather than simple magnitude thresholds. This expansion of command capacity is pivotal for simplifying resistive readout interfaces and reducing wiring complexity, allowing a single sensor node to execute multifunctional tasks that would otherwise require complex arrays[14]. Crucially, pioneering efforts in resistive sensing have explored various anisotropic architectures and microfracture mechanisms to achieve such directional self-decoupling[15-17]. For instance, Kim *et al*. investigated the dynamic opening-closing behaviors of crack-based sensors to distinguish between convex and concave strains[18], while Wang *et al*. developed planar "spiderweb" slit structures to decouple multidirectional forces via geometric design[19]. Although these innovative strategies successfully encode diverse mechanical inputs into distinctive electrical signals under dry conditions, they share a critical dependency on surface-dominated structural reconfigurations[20]. In particular, the sensing mechanism fundamentally requires mechanical freedom at the interface regardless of whether microcrack propagation or structural buckling is used[21,22]. This dependency creates a fatal paradox when transitioning to amphibious environments. To survive underwater or sweat-rich conditions, sensors typically require thick extrinsic encapsulation [e.g., polydimethylsiloxane (PDMS) or ecological flexibility (EcoFlex)][23-25]. However, this protective layer acts as a parasitic mechanical clamp that physically restricts, or even fills, the sensing gaps[26,27]. Unlike bulk piezoresistive composites that rely on internal lattice deformation, these surface-sensitive microstructures are effectively frozen by encapsulation, severely dampening the differential contact resistance required for ternary logic. Consequently, an amphibious interface that simultaneously retains high-fidelity directional perception and achieves intrinsic environmental immunity without sensitivity-degrading encapsulation is required.

The semiaquatic fishing spider (*Dolomedes*) provides a natural evolutionary model for resolving the fundamental conflict between environmental isolation and mechanical sensitivity [Figure 1A][28]. This arachnid is uniquely adapted to the metastable air-water interface and overcomes the protection-sensitivity

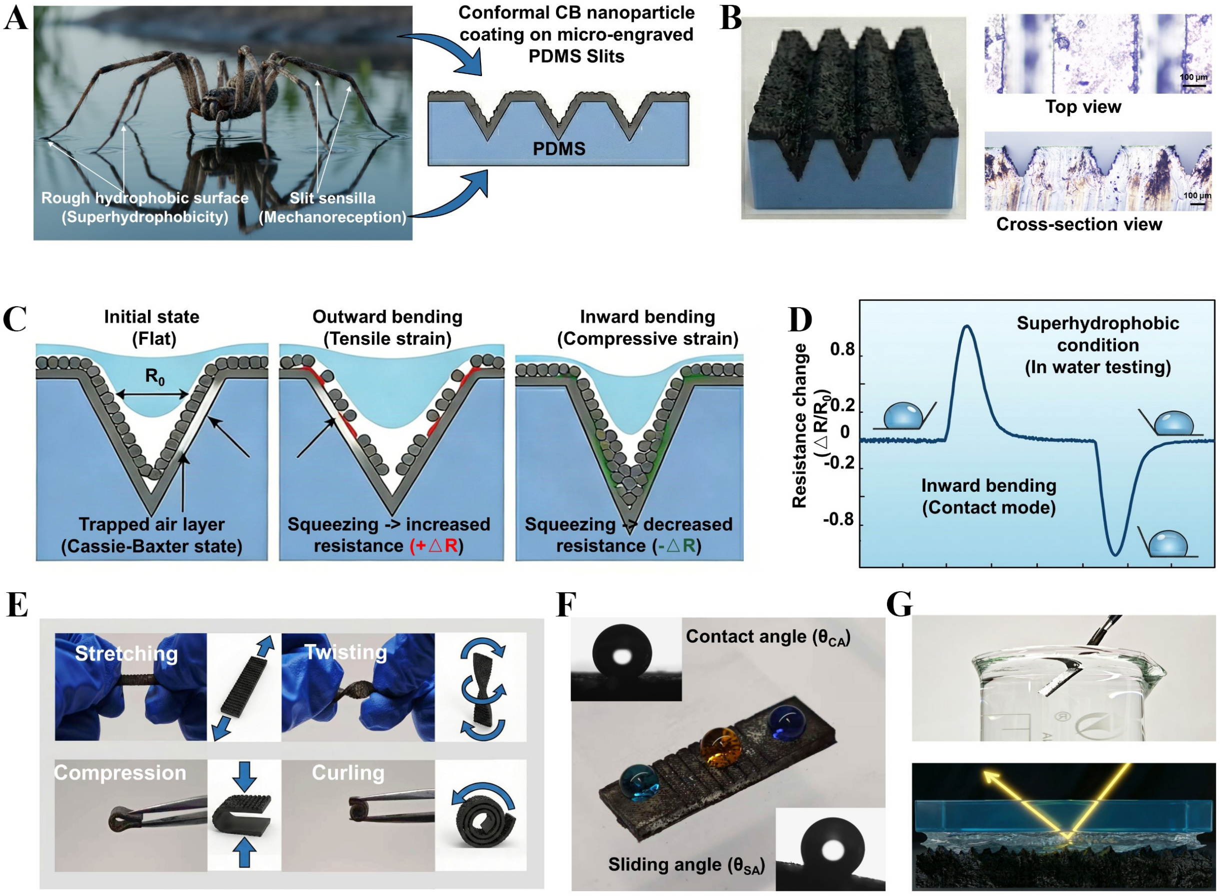

Figure 1. Bioinspired design strategy and electromechanical working principle of the monolithic superhydrophobic sensor. (A) Schematic of the biomimetic mapping of the fishing spider, translating its biological slit sensilla (mechanoreception) and hierarchical microsetae (superhydrophobicity) into a microengraved PDMS/CB architecture; (B) Schematic and optical microscopy images showing the macroscopic slit array, microscopic surface roughness (top view), and deep-groove profile (cross-sectional view); (C) Illustration of the bidirectional sensing mechanism under outward and inward bending, featuring a stable air-plastron interface; (D) Representative real-time resistance response curves corresponding to the bidirectional deformation modes; (E) Photographs demonstrating the mechanical flexibility of the sensor under stretching, twisting, compression, and curling; (F) Surface wettability characterization showing a high static water contact angle and low sliding angle with multicolored liquid droplets; (G) Underwater optical photograph of the air plastron, showing the characteristic "silver mirror" reflection. CB: Carbon black; PDMS: polydimethylsiloxane.

tradeoff through structural monism. Functionally, it relies on exposed slit sensilla (microcracks) for mechanoreception; structurally, the very surface of these sensors is patterned with hierarchical microsetae to trap a stable air pocket upon water contact[29]. Here, the trapped air layer serves as an "invisible gaseous armor" that physically isolates the sensory slits from liquid interference[30]. This gaseous barrier is established directly atop the sensory structure without imposing any solid impedance, thereby ensuring that the microcracks retain full motional freedom and direct physical interaction capabilities even under full submersion[31].

While recent advancements have successfully employed intrinsic superhydrophobic interfaces to replace thick encapsulation, these approaches still require an insulating coating[32]. In particular, conventional superhydrophobic fabrication typically involves modifying surfaces with low-surface-energy fluoropolymers or nanoparticles to achieve water repellency. While structurally effective, these agents are predominantly electrically insulating[33]. Notably, advanced manufacturing techniques, such as laser-induced surface engineering, have demonstrated the capability to create high-performance conductive and water-repellent architectures directly on various functional substrates[34]. Complementary to these sophisticated physical strategies, there is significant interest in developing integrated chemical-mechanical routes specifically optimized for soft elastomeric matrices. For sensors that rely on the precise "crack closure" and electron percolation between conductive walls, such a coating introduces a parasitic dielectric interface[34,35]. When the sensor is compressed, this insulating layer prevents direct electrical contact between the crack sidewalls, severing the conductive network reconstruction required for ternary logic. Therefore, the challenge lies not merely in creating a superhydrophobic surface, but in engineering a unified architecture where the conductive material itself possesses superhydrophobicity, allowing for simultaneous water repellency and high-fidelity electroactive contact[23].

Guided by this encapsulation-free bio-model, we report a monolithic superhydrophobic sensor fabricated via a facile mechanical microengraving and solvent-assisted swelling strategy. Distinct from coating-based approaches that create insulating layers, we use a swelling process to embed conductive carbon black (CB) nanoparticles directly into the PDMS matrix of mechanically microengraved microslits. This technique simultaneously constructs a robust conductive percolation network and a hierarchical surface roughness. Functionally, the unique slit architecture enables distinct bidirectional mechanotransduction wherein outward bending induces crack separation (increasing resistance), while inward bending triggers contact reconstruction (decreasing resistance), allowing for the clear differentiation of bending directions (± 8° to 60°) with a rapid response time (rise and recovery times of 240 and 200 ms, respectively). Crucially, the intrinsic superhydrophobicity (contact angle of > 153°) ensures exceptional robustness, preserving the structural integrity, self-cleaning capability, and electrical fidelity. Specifically, the sensor maintains a stable electromechanical performance over 500 cycles in harsh conditions, including acidic, alkaline, and dusty environments, where traditional exposed slit-sensors typically fail. Finally, we demonstrate a ternary-logic (3^n) interaction system and a "aquatic phantom" underwater robotic skin by leveraging the positive/negative signal capacity of the device. Our findings validate the potential of this sensor for high-capacity, environment-adaptive intelligent perception.

EXPERIMENTAL

Materials

A PDMS prepolymer and curing agent (Sylgard 184) were purchased from Dow Corning (USA). CB nanoparticles (VXC-72R, average diameter of ~30 nm) were acquired from Cabot Corporation (USA). Cyclohexane (C_6H_{12}, analytical grade) was obtained from Damao Chemical Reagent Factory (Tianjin, China). Hydrochloric acid (HCl), sodium hydroxide (NaOH), and sodium chloride (NaCl) were purchased from Sinopharm Chemical Reagent Co., Ltd., for the environmental durability and self-cleaning tests. In addition, quartz sand was employed to evaluate the contaminant-repellent properties. All chemicals were used as-received without further purification.

Preparation of the bidirectional superhydrophobic stain sensor

The monolithic fabrication of the bioinspired sensor was achieved through the facile integration of mechanical microengraving and a solvent-assisted swelling strategy. Initially, a PDMS substrate (10 mm × 5 mm × 2 mm) was molded from a computer numerical control (CNC)-machined poly(methyl methacrylate) template using a standard precursor mixture (5:1 mass ratio), followed by degassing and thermal curing at 80 C for 30 min. To replicate the mechanosensitive geometry of spider slit sensilla, the cured substrate was remounted onto the CNC system, where a tapered blade created precise microslits. Crucially, the fabrication parameters, specifically the slit depth and number of parallel slits, were systematically varied during this step to optimize the electromechanical response. Following engraving, the device underwent a one-step functionalization process by immersing it in a CB/cyclohexane suspension (0.02 g mL^{-1}) under ultrasonication (~ 150 W) for 2 h. Cyclohexane-induced swelling temporarily dilates the PDMS molecular network to facilitate the deep infiltration of CB nanoparticles. Upon solvent evaporation, the network contracts to intrinsically anchor these conductive fillers, resulting in the conformal and dense accumulation of CB agglomerates on the slit surfaces. The volumetric swelling ratio (SR_v) was monitored through dimensional variations and is defined as $SR_v = (V_s - V_d) / V_d$, where V_s and V_d are the sample volumes in the swollen and dry states, respectively. The SR_v value obtained during this expansion process reached 2.03 ± 0.24 (mean ± SD; $N = 4$) before returning to a stable state. After rinsing and drying, the resulting sensor possessed a robust, monolithic conductive network integrated with a hierarchical superhydrophobic surface, eliminating the need for additional adhesive layers.

Characterization and measurement

The surface morphologies and cross-sectional microstructures were examined using scanning electron microscopy (SEM; Nova NanoSEM450, USA). Additionally, the macroscopic structural integrity and slit distribution were observed using high-resolution optical microscopy (OM; Shunyu Optics Technology Group Co., Ltd., MX6R, China). The surface wettability was quantified by measuring the static water contact angle (θ_{CA}) and sliding angle (θ_{SA}) using a contact angle goniometer (OSA100S-T, Ningbo NB Scientific Instruments Co., Ltd., China), and average values were derived from 10 μL droplets at five distinct locations. A comprehensive durability assessment was conducted to rigorously validate the environmental and mechanical robustness of the sensor for amphibious applications. The mechanical stability was evaluated through tape-peeling tests (standard 3M tape), sandpaper abrasion (2000 grit), and high-speed water-jet impact, wherein θ_{CA} and θ_{SA} were monitored to detect wettability degradation. Chemical and environmental immunity were assessed by exposing the sensor to ultraviolet (UV) irradiation. Furthermore, the universal liquid repellency was verified via comparison with complex fluids including milk, juice, and cola, as well as acidic (HCl, pH = 2), alkaline (NaOH, pH = 12), and saline (NaCl, 3.5 wt.%) solutions. In addition, dynamic wettability was evaluated under uniaxial tensile strains ranging from 0% to 100% to ensure functional stability under deformation.

For real-time electrical signal acquisition, the sensor terminals were connected using conductive silver paste and copper foil tape to ensure minimal contact resistance. These connections were mechanically reinforced with encapsulation tape to prevent detachment during deformation. The sensor was mounted onto a flexible polyethylene terephthalate (PET) substrate, which served as a supporting cantilever to convert linear motor displacement into defined bending angles. Here, one end of the PET substrate was fixed, while the other was clamped to the moving arm of a motorized bidirectional bending test system (Mark-10, China). As the motor moved, the substrate underwent controlled bending. This setup allowed for bidirectional testing as “outward bending” and “inward bending” were achieved by reversing the mounting orientation relative to the bending direction. The real-time resistance variations were recorded using a high-precision digital multimeter (B2902A, Keysight, USA) interfaced with a computer. To evaluate long-term fatigue resistance, the device was subjected to 500 continuous bending cycles at a frequency of 0.1 Hz within a bending angle range of ± 8°. The dynamic response time and recovery capability were characterized by applying instantaneous step strains and monitoring the signal delay. The temperature-dependent stability experiments were conducted on a heating plate, and the sensors were characterized across a temperature range of 20-70 °C. All experimental data were recorded, processed, and analyzed using OriginPro 2016 software (OriginLab Corp., USA).

The wearable and underwater demonstrations were performed by a research volunteer under strict safety protocols, and informed consent was obtained prior to the study. Tests with volunteers were conducted in compliance with ethical regulations under a protocol approved by the Scientific Research Ethics Committee of School of Integrated Circuits of Shandong University (approval number KJLL-2024-01-006). The sensor was adhered to various locations on the human body to evaluate the wearable sensing performance. During physical activity, a digital multimeter recorded real-time resistance variations to characterize human-mechanical behaviors. For underwater sensing applications, the sensor was mounted onto the wrist and finger joint of the volunteer. Sensing signals were successfully captured in real-time within the aquatic environment by establishing an electrical connection with a peripheral digital multimeter. In addition, a customized HMI system was developed for real-time robotic vehicle control to evaluate the ternary sensing strategy. Two bidirectional sensors were interfaced with an STM32 microcontroller, which sampled resistance variations at a frequency of 1×10^{-3} Hz. The raw data were transmitted via a serial port to a terminal, where a custom Python script encoded the signals into ternary states (1, 0, or -1) based on the bending direction and magnitude, corresponding to the nine states of the vehicle on the interface. The application scope of the sensor was then further extended to underwater reconnaissance, focusing on contact detection and spatial localization. An experimental platform was constructed using a programmable engraving machine to precisely control the lateral scanning movement of the sensor across a submerged target. The inherent bidirectional sensitivity allowed for the discrimination of the relative position of the object as an outward bending deformation during leftward motion produced a positive resistance response, while inward bending deformation during rightward motion yielded a negative signal. These real-time variations were processed via a Python-based graphical user interface (GUI). The system remained in a "SAFE" state during idle periods and immediately triggered a "WARNING" status upon physical contact, and the contact trajectory was dynamically plotted to visualize the spatial coordinates of the target.

RESULTS AND DISCUSSION

The semiaquatic fishing spider, *Dolomedes*, is a specialized arachnid that thrives at the metastable water-air interface. The spider uses its slit sensilla to survive and hunt effectively in this dual environment, which function as highly sensitive strain detectors located near its metatarsus and tarsus bones to detect minute vibrations generated by prey ripples. Simultaneously, its exoskeleton is covered in densely arranged microsetae with heights ranging from tens to hundreds of micrometers that exhibit extreme surface hydrophobicity and trap an insulating air layer to repel water and prevent drowning. While these two crucial functions are executed by separate anatomical features in the spider, their synergistic coexistence provides a profound inspiration for amphibious sensing. Guided by this biological integration, we designed a monolithic sensor architecture that unifies high-fidelity sensing with intrinsic environmental immunity [Figure 1A]. The fabrication process employs a facile mechanical microengraving technique followed by a solvent-assisted swelling strategy, and it is detailed in Supplementary Figure 1 and Video 1. This process results in a monolithic encapsulation-free structure that ensures a tighter integration and prevents delamination under mechanical stress. The resulting morphological features are presented in Figure 1B, wherein the array of precise, V-shaped microslits created by the tapered blade is shown. Further SEM analysis highlights the monolithic nature of the device [Supplementary Figure 2]. The surface SEM image shows a dense and uniform distribution of CB particles, while the cross-sectional view verifies that these conductive fillers are fully embedded within the PDMS matrix, creating a cohesive functional unit without encapsulation. Meanwhile, the CB nanoparticles themselves exhibit intrinsic hydrophobicity. Predominantly composed of sp^2-hybridized carbon, CB features a surface rich in nonpolar C-C bonds and aromatic domains, with negligible polar hydrophilic groups such as -OH and -COOH. This leads to weak intermolecular affinity with polar water molecules, giving CB an inherent hydrophobic character. As a result, the CB/PDMS superhydrophobic self-decoupling ternary sensor fabricated by embedding CB nanoparticles exhibits hydrophobicity on its surface. Additionally, PDMS is a widely recognized low-surface-energy polymer with intrinsic hydrophobicity, and this further contributes to the superhydrophobicity of the composite sensor.

The obtained morphology provides the structural foundation for the coupled bidirectional sensing and environmental stability illustrated in Figure 1C. In the initial state, the rough conductive sidewalls maintain a loose, percolation-threshold contact, establishing a stable baseline resistance (R_0). Simultaneously, this hierarchical roughness supports a stable Cassie-Baxter state, trapping an insulating air layer within the microcavities to isolate the electrical pathways from liquid intrusion. The fundamental sensing mechanism is governed by the reversible variation in the conductive contact area and the dispersion status of the conductive particles across these microslits. Under outward bending, the V-shaped slits undergo geometric expansion, separating the opposing sidewalls. This physical separation disrupts the preexisting conductive percolation network among the CB nanoparticles, resulting in a sharp increase in resistance (positive signal, $+\Delta R$). Conversely, inward bending exerts a squeezing effect that forces the rough sidewalls into intimate interlocking contact. This action significantly expands the effective electroactive area and creates new percolation paths through the densified CB network, resulting in a distinct decrease in resistance (negative signal, $-\Delta R$). Crucially, throughout these mechanical deformations, the hierarchical roughness ensures that the air plastron remains intact, preserving superhydrophobicity even as the crack geometry changes. This unique electromechanical behavior allows for the intrinsic discrimination of deformation direction while maintaining environmental immunity. As demonstrated in the real-time response curves shown in Figure 1D, the sensor produces distinguishable signal polarities, effectively decoupling convex and concave deformations without requiring complex signal-processing algorithms. Macroscopically, the device operates as a highly sensitive bidirectional bending sensor. However, this bending deformation is a manifestation of vectorial microstrains on the substrate surface. According to the principles of continuum mechanics, outward (convex) bending subjects the top-surface microslits to localized tensile strain. This leads to the physical separation of the conductive network and a positive resistance change ($+\Delta R$). Conversely, inward (concave) bending induces compressive strain, which densifies the conductive pathways and yields a negative resistance change ($-\Delta R$). By effectively decoupling these vectorial microstrains, our monolithic architecture translates macroscopic bending behaviors into distinct, directional electrical signals. Notably, the water droplets residing on the sensor surface maintain a high contact angle throughout both bidirectional bending states, verifying that the dynamic sensing process does not compromise the superhydrophobic integrity established by the bioinspired architecture.

The developed sensor demonstrates mechanical flexibility owing to its fabrication using an encapsulation-free method. As depicted in Figure 1E, the elastomer-based device can withstand various complex deformations, including stretching, twisting, compression, and curling, without structural degradation or delamination of the conductive network. Furthermore, the hierarchical surface roughness endows the sensor with intrinsic superhydrophobicity. As characterized in Figure 1F, liquid droplets (dyed for visibility) deposited on the surface spontaneously adopt a spherical geometry, indicative of the stable Cassie-Baxter state. Quantitative measurements confirm a high static contact angle (C_{CA}) exceeding 153° and a low sliding angle (C_{SA}) of less than 10°. This low surface adhesion further imparts an excellent self-cleaning capability; as demonstrated in Supplementary Figure 3, contaminants such as sand can be easily carried away by rolling water droplets, mimicking the lotus effect and maintaining the surface cleanliness required to ensure long-term reliability in slit-based sensors. In traditional exposed sensors, the accumulation of microscopic dust or contaminants within the sensing gaps often leads to irreversible structural fouling and signal drift. By leveraging the bioinspired lotus effect, the hierarchical surface of the developed sensor ensures that rolling droplets effectively remove surface debris before they can clog the microchannels.

The existence of a stable air-solid interface is most vividly evidenced by the underwater optical test results presented in Figure 1G. When the sensor is fully submerged in water, its surface exhibits a prominent "silver mirror" reflection. This optical phenomenon arises from the total internal reflection of light at the interface between the water and the trapped air layer. This observable air plastron confirms that the hierarchical microgrooves successfully entrap a continuous gaseous barrier, which physically isolates the sensing elements from the surrounding aqueous environment, thereby ensuring the electrical stability of the sensor during amphibious operation.

To elucidate the high sensitivity required for precise signal discrimination, we analyzed the equivalent circuit model of the microslits [Figure 2A]. Unlike planar films that rely on superficial crack propagation, the deep V-shaped groove architecture functions as a geometric amplifier for resistance variation. Physically, the deep trenches significantly expand the specific surface area, allowing for a conformal and dense packing of CB nanoparticles. Electrically, this structure acts as a variable resistor dominated by the sidewall contact width (W). As illustrated in Figure 2A, the resistance modulation is governed by the drastic variation in this effective conductive area: under inward bending, the contact width macroscopically expands from W_0 to $W + \Delta W$, creating a robust low-resistance pathway; conversely, under outward bending, the separation of these densely packed sidewalls severs the conductive network. This geometric amplification mechanism ensures that even small deformations translate into substantial resistance shifts, generating the distinct positive/negative signals visualized in Figure 2B. Based on this mechanism, a structural optimization strategy was implemented by varying the number of parallel slits to tune the sensitivity of the sensor [Figure 2C]. As the number of slits (N) increases from one to nine, the device effectively acts as a series of variable resistors. Consequently, the cumulative disconnection (tensile strain) or contact reconstruction (compressive strain) of multiple conductive paths leads to a superposition of resistance changes. The quantitative analysis shown in Figure 2D confirms that the relative resistance change ($\Delta R/R_0$) increases linearly with the slit density, verifying that the multislit design effectively amplifies the mechanotransduction signal. Therefore, the device with nine parallel slits was selected for all subsequent characterizations. The optimized sensor exhibits excellent electromechanical performance characteristics. Furthermore, it was found that the depth of the microchannel significantly influences sensor sensitivity [Supplementary Figure 4]. While increasing the depth initially boosts the resistive response by allowing for greater structural deformation, exceeding an optimal depth of 200 μm leads to diminishing returns as the flexible base can no longer fully deform into the deepened V-shaped geometry.

The optimized sensor demonstrates excellent electromechanical characteristics suitable for logic control. The initial and flexed states of the sensor, along with the governing equations for calculating the bending angle, are provided in the Supporting Information [Supplementary Figure 5 and Note 1]. The resistance response curve [Figure 2E] reveals four distinct linear regions with tunable gauge factors (GFs), ensuring reliable sensitivity across a broad deformation range. Specifically, the GFs relate to the relative change in resistance normalized against the angular strain, where the unit angle is defined as the ratio of the central angle (α) of the device to the maximum possible bending central angle (180°). Based on this definition, the sensor exhibits a high sensitivity with a maximum GF of approximately 7.1 in both bending directions. Notably, the high sensitivity ($GF \approx 7.1$) of our sensor is fundamentally preserved by its monolithic and encapsulation-free architecture. In addition, the proposed sensor decouples environmental protection from mechanical constraints by using a stable gaseous air plastron as a frictionless barrier instead of the solid coating used in conventional flexible sensors. This system preserves the full motional freedom of the conductive network. Dynamic testing under cyclic stretching-releasing (8° to 28° bending angles) confirms that the sensor maintains stable and distinguishable signal amplitudes without degradation [Figure 2F]. Regarding real-time interaction, the device exhibits a rapid rise and recovery times of 240 and 200 ms, respectively [Figure 2G], which are sufficient for capturing dynamic human motions. A similar rapid performance was observed during inward bending [Supplementary Figure 6], confirming the high-speed bidirectional transduction capability of the encapsulation-free sensing network. Furthermore, step-hold tests [Figure 2H] highlight the exceptional linearity and stability of the sensor. The electrical output tracks the stepwise deformation with high precision, as evidenced by the high determination coefficients ($R^2 > 0.97$) for both the loading and unloading phases. This linear correlation, combined with negligible mechanical hysteresis and signal drift, validates the ability of the sensor to maintain the stable and predictable logic states required for ternary interaction systems. Finally, the dynamic response remains consistent across varying frequencies (0.05 and 0.1 Hz) and amplitudes [Figure 2I and J], demonstrating a reliable frequency-independent performance essential for complex task monitoring.

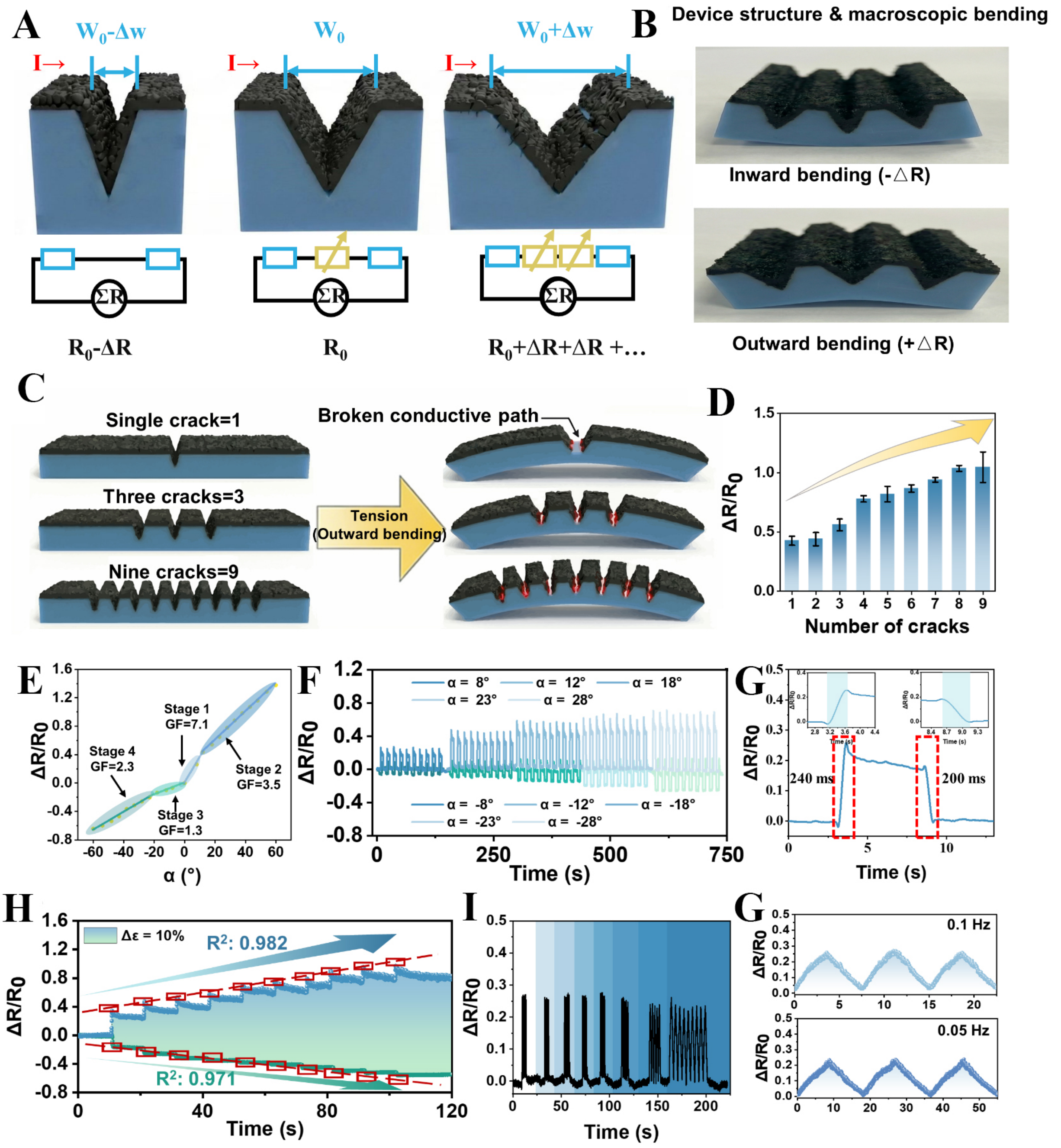

Figure 2. Working mechanism and electromechanical performance optimization of the bidirectional sensor. (A) Schematic and equivalent circuit model showing the fundamental resistance-variation mechanism. Inward bending increases the sidewall contact width, decreasing resistance, while outward bending separates the crack surfaces, increasing resistance; (B) Schematic showing the device undergoing inward (negative signal) and outward (positive signal) bending deformations; (C) Schematic of the structural optimization strategy achieved by increasing the number of parallel microslits from one to nine to enhance signal magnitude; (D) Quantitative analysis results of the relative resistance change as a function of slit number; (E) Characteristic bending central angle (α)-resistance curve identifying four distinct linear regions with corresponding GFs, demonstrating stable bidirectional sensitivity. The values are presented as mean ± SD; N = 5; (F) Real-time electrical response under cyclic stretching and releasing at varying α amplitudes (8° to 28°); (G) Transient response showing rapid rise (240 ms) and recovery (200 ms) times during an outward bending cycle; (H) Step-hold strain testing demonstrating the signal stability and low mechanical hysteresis during stepwise loading and unloading phases; (I) Dynamic resistance response obtained under variable deformation frequencies and amplitudes; (J) Signal consistency verification obtained at different actuation frequencies (0.1 and 0.05 Hz). GF: Gauge factor; SD: stand deviation.

Constructing a stable solid-air-liquid interface is a prerequisite for amphibious sensing to prevent signal distortion caused by liquid leakage. Structurally, this capability is ensured by the hierarchical dual-scale architecture in the proposed sensor, in which the microscale engraved ridges and nanoscale CB agglomerates synergistically form a robust superhydrophobic barrier. Figure 3A illustrates the mechanism of this contact-based superhydrophobicity as the micro-nano composite structures effectively trap an insulating air cushion, supporting liquid droplets in a stable Cassie-Baxter state. The optical images shown in Figure 3B corroborate this state as they show a spherical water droplet resting on the sensor surface with a microscopic roughness profile that minimizes the solid–liquid contact area. We conducted comprehensive durability assessments to evaluate the longevity of this air plastron under dynamic operating conditions. Figure 3C presents the evolution of θ_{CA} over 800 continuous bending cycles (± 60°). While the initial θ_{CA} is measured at > 153°, the sensor exhibits negligible degradation during testing, indicating excellent long-term surface stability against mechanical fatigue. Similarly, maintaining water repellency under large deformations is critical as the sensor is designed for flexible electronics. As shown in Figure 3D, θ_{CA} remains virtually unchanged even when subjected to dynamic uniaxial tensile strains ranging from 0% to 100%. We attribute this robust deformability to the dense and conformal packing of the CB nanoparticles anchored by the swelling strategy, which ensures that the hierarchical roughness is preserved without cracking or detaching even under significant geometric distortions.

The mechanical robustness of the conductive superhydrophobic layer, which is often the weak point of conventional coatings, was rigorously evaluated. The exceptional durability of the proposed sensor is attributed to the solvent-assisted swelling strategy, which deeply anchors the CB nanoparticles within the PDMS matrix. Tape-peeling tests [Figure 3E] demonstrate that the surface maintains high θ_{CA} and low θ_{SA} values even after repeated peeling cycles, verifying the strong cohesive adhesion of the functional layer. Simultaneously, the electrical resistance variations were monitored during these destructive tests [Supplementary Figure 7]. After the initial peeling cycles, the rate of resistance change began to decline, which might be attributed to the abscission of the CB nanoparticles adhering to the surface. Subsequently, 90 destructive experiments were conducted, all of which resulted in small resistance fluctuations and confirmed the presence of the intact conductive network within the matrix. Similarly, the sensor withstood severe abrasion against sandpaper [Figure 3F] and high-speed water jet impacts [Figure 3G] with minimal wettability loss, verifying its resistance toward friction-induced wear and dynamic hydraulic pressure. In addition to physical resilience, the resistance of the sensor toward environmental and chemical aggressors was verified to ensure survival in real-world scenarios. Resistance to photooxidation was confirmed by UV-light irradiation tests [Figure 3H], where the surface retained its superhydrophobicity, simulating resilience against long-term outdoor sunlight exposure. Moreover, the sensor demonstrated universal repellency against various complex and corrosive fluids. As depicted in Figure 3I, droplets of water, milk, and juice, as well as strong acid (HCl), alkali (NaOH), and salt (simulating seawater) solutions, all retained spherical shapes on the sensor surface without wetting it. Crucially, the superhydrophobic surface facilitates the formation of a stable air plastron during complete immersion, which acts as an effective barrier against ionic infiltration. This unique interface ensures that the electromechanical signals remain stable even in corrosive environments containing acids, bases, or salts [Supplementary Figure 8]. In addition, it prevents water from infiltrating the microslits, thereby eliminating hydraulic capillary locking and the liquid-induced damping that typically suppress the sensitivity of contact-based sensors. This ensures that the sensing microstructures retain their full mechanical freedom to open or close, preserving the same high-fidelity mechanotransduction as observed in dry conditions.

Building upon the robust environmental immunity established in the static tests, we further evaluated the capability of the sensor for real-time human-motion monitoring in complex amphibious environments. A critical challenge affecting unencapsulated wearable sensors involves preventing signal distortion caused by the surrounding medium, particularly in aquatic settings where water and dissolved ions can induce short circuits. Figure 4A illustrates the fundamental protection mechanism enabled by the design of the proposed

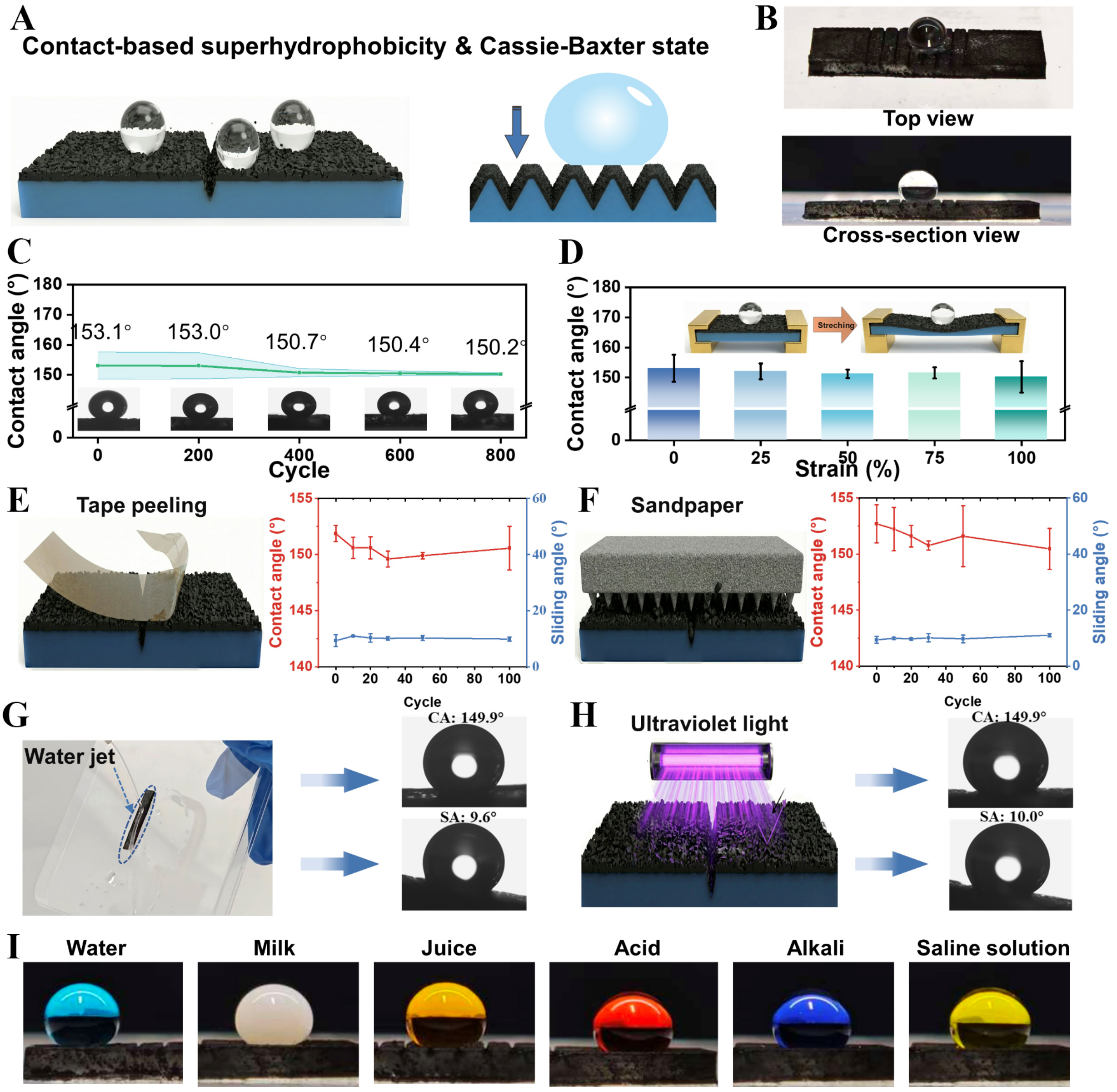

Figure 3. Characterization of the robust superhydrophobic surface and environmental durability of the proposed sensor. (A) Schematic of the superhydrophobicity and air cushion in the Cassie-Baxter state; (B) Optical images showing a water droplet residing on the sensor surface (top view) and the microscopic roughness profile (cross-sectional view); (C) Long-term durability assessment showing the evolution of the θ_{CA} over 800 bending cycles (± 60°). The values are presented as mean ± SD; *N* = 3; (D) Variation of the θ_{CA} under dynamic uniaxial tensile strains ranging from 0% to 100%; (E) Tape-peeling test results displaying the evolution of θ_{CA} and θ_{SA} over repeated peeling cycles. The values are presented as mean ± SD; *N* = 3; (F) Sandpaper abrasion test characterization showing the retention of high θ_{CA} and low θ_{SA} values against friction-induced wear. The values are presented as mean ± SD; *N* = 3; (G) High-speed water-jet impact test demonstrating resistance to dynamic liquid pressure, with minimal degradation in θ_{CA}/θ_{SA} values after impact; (H) UV-light irradiation test simulating resilience against long-term outdoor aging; (I) Optical images of various complex fluids, including water, milk, juice, and acid, alkali, and salt (simulating seawater) solutions, maintaining spherical shapes on the sensor surface. θ_{CA}: Contact angle; θ_{SA}: sliding angle; SD: stand deviation; UV: ultraviolet.

sensor. Unlike exposed sensors that suffer from ionic crosstalk, the trapped air plastron on the superhydrophobic surface of the proposed sensor acts as a physical dielectric barrier. This gaseous layer effectively isolates the sensing microcracks from the external environment, shielding the conductive percolation network from interference via the conductive ions present in the water. To validate this mechanism during dynamic movement, we monitored finger and wrist bending under three distinct conditions: dry, humid (simulating sweat), and fully submerged. As shown in Figure 4B and C, the sensor produced consistent resistance response waveforms across all environments. The absence of significant signal distortion or baseline shifts in the submerged state confirms that the air plastron remains stable even under joint deformation, ensuring reliable amphibious monitoring without bulky external encapsulation.

Beyond environmental stability, the sensor addresses a core requirement of advanced HMI, namely the recognition of high-dimensional joint kinematics. As shown in Figure 4D, the human anatomical landscape involves a complex interplay of joints with varying degrees of freedom, ranging from simple hinge joints to complex multiaxial pivots. Traditional resistive sensors, which typically output only positive resistance changes upon stretching, struggle to distinguish between antagonistic movements (e.g., flexion *vs.* extension) without deploying sensor arrays. The proposed sensor provides a simplified solution for decoupling these motion directions via its unique bidirectional mechanotransduction mechanism [Figure 4E-H]. For unidirectional joints such as the elbow and knee, which primarily undergo skin-stretching during actuation, the sensor exhibits a standard strain-sensing behavior, translating flexion angles into proportional positive resistance changes ($+\Delta R$). More importantly, for bidirectional joints such as the finger and wrist, the device demonstrates an exceptional capability to intrinsically distinguish motion polarity. The magnitude of these signals linearly corresponds to the specific bending angles (e.g., $0° \rightarrow \pm 30° \rightarrow \pm 60°$), allowing for the precise reconstruction of joint vectors. Finally, to validate the suitability of this device for long-term wearable applications, a cyclic fatigue test was conducted [Figure 4I]. The sensor maintained stable electrical fidelity over 500 cycles, demonstrating the excellent mechanical durability and signal repeatability required for practical, long-duration HMIs [Supplementary Videos 2-7]. The electromechanical response of the sensor was also tested from 20 to 70 °C to evaluate its thermal stability [Supplementary Figure 9]. The monolithic architecture ensures a highly stable baseline by deeply anchoring the CB nanoparticles, which restricts thermally induced microsliding. In particular, any dimensional changes caused by thermal expansion are negligible compared to the macroscopic strain applied during operation. This ensures consistent sensitivity and highlights the potential of this sensor for use in diverse thermal environments.

Beyond physiological monitoring, HMIs represent a critical application domain for wearable electronics.[36-39] However, conventional resistive sensors typically function as binary switches, producing a high signal (“1”) under stimulation and a low signal (“0”) in the absence of input. Consequently, an array of n binary sensors is limited to a command capacity of 2^n [Figure 5A], which restricts the complexity of control protocols. By contrast, our bidirectional sensor intrinsically encodes mechanical stimuli into three mutually exclusive output states [Figure 5B]. The “1” state is physically governed by the crack-opening mechanism under outward bending, which leads to a positive resistance increment ($\Delta R/R_0 > 0$). By contrast, the “-1” state is driven by the structural densification and the enhancement of conductive pathways under inward bending, resulting in a negative resistance change ($\Delta R/R_0 < 0$). Finally, the “0” state strictly represents the initial equilibrium or relaxed phase of the sensor ($\Delta R/R_0 = 0$). This additional degree of freedom fundamentally upgrades the system to a ternary-logic architecture, expanding the command capacity to 3^n using the same number of sensor nodes. To demonstrate this high-density command capability, we constructed a prototype HMI system using two identical bidirectional sensors attached to the user’s fingers. As illustrated in Figure 5C and D, this dual-sensor configuration ($n = 2$) generates nine distinct logic combinations. We defined a custom coding protocol to map these states to the maneuvering of a virtual racing car. For instance, when both sensors remain idle (0, 0), the vehicle remains stationary [Figure 5E]. By manipulating the bending direction of individual fingers, specific vectors are generated: keeping Sensor 1 idle while flexing Sensor 2 inward (0, -1) triggers a “stationary left turn” [Figure 5F], whereas extending Sensor 1 outward while flexing Sensor 2 inward (1, -1) executes a complex “forward right turn” maneuver [Figure 5G]. Furthermore, the simultaneous outward extension of both sensors (1, 1) is mapped to a “backward left turn” command [Figure 5H]. As further demonstrated in Supplementary Video 8, this ternary strategy significantly enriches the command space without increasing hardware complexity, providing a scalable and efficient strategy for next-generation, minimalist HMI systems.

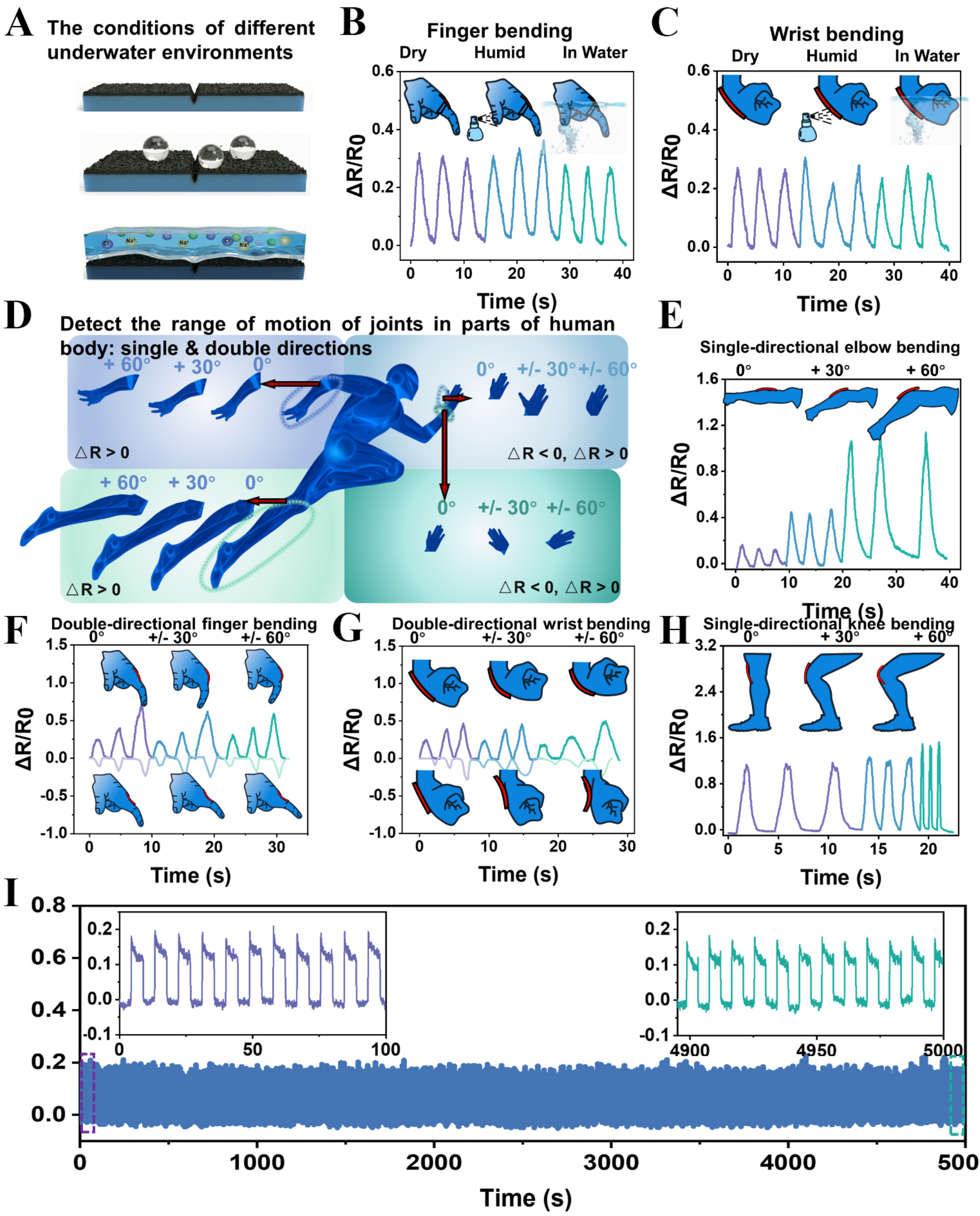

Figure 4. Demonstration of amphibious human-motion monitoring and multidimensional joint recognition. (A) Schematics of the three testing conditions: dry, humid, and fully submerged. Real-time resistance responses of (B) finger and (C) wrist bending under these varying conditions; (D) Schematic mapping of human body joints, categorizing them into unidirectional (elbow, knee) and bidirectional (finger, wrist) kinematic ranges; (E) Elbow and (H) knee bending produce only positive resistance changes, corresponding to outward skin-stretching at varying angles; (F) Finger and (G) wrist bending demonstrating the capability to decouple motion direction as inward flexion triggers a resistance decrease while outward extension triggers a resistance increase. In addition, distinct signal amplitudes corresponding to specific bending angles (0° → ± 30° → ± 60°); (I) Long-term cyclic stability test performed over 500 cycles of continuous bending at 0.1 Hz (± 8°).

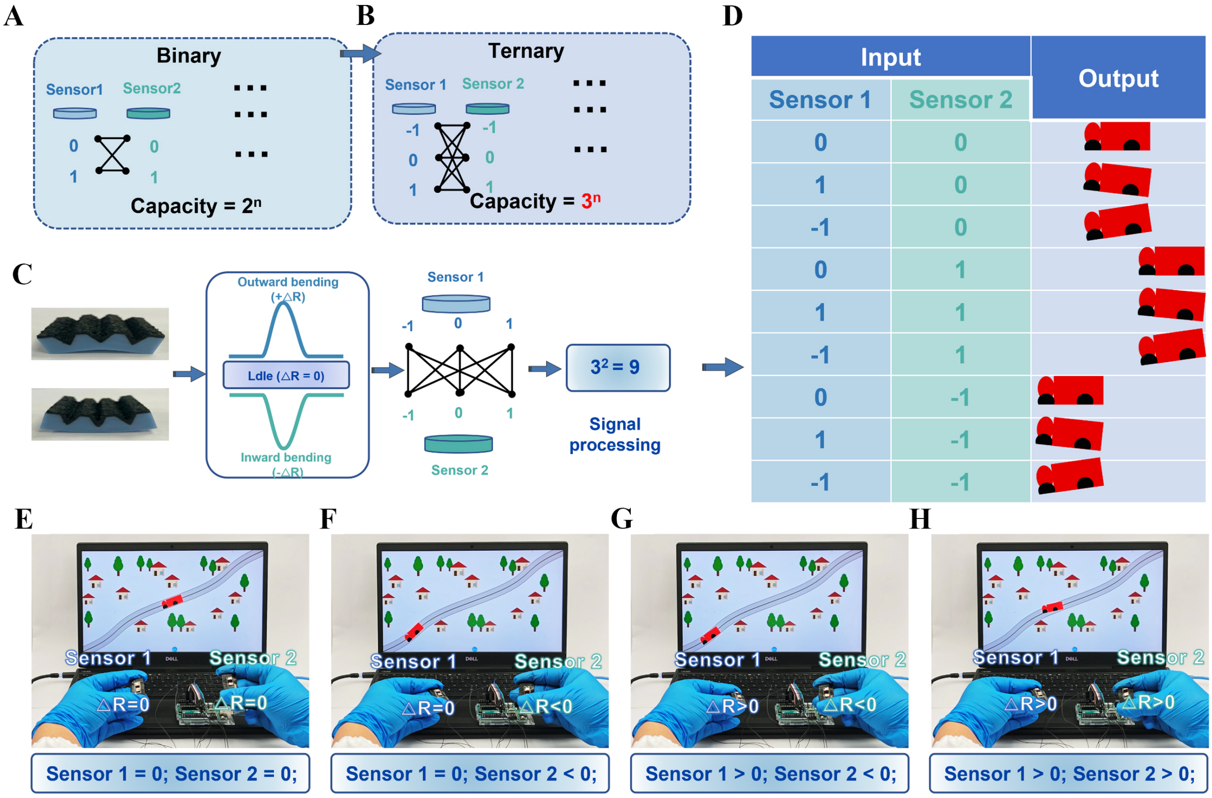

Input		Output
Sensor 1	Sensor 2	
0	0	
1	0	
-1	0	
0	1	
1	1	
-1	1	
0	-1	
1	-1	
-1	-1	

Figure 5. Demonstration of the ternary-logic interaction system for high-dimensional HMI control. (A) Traditional binary logic systems (2^n) and (B) the proposed ternary-logic system (3^n); (C) Two bidirectional sensors generate three discrete states based on deformation mechanics including "1" (outward bending, +Δ*R*), "0" (idle, stable R_0), and "-1" (inward bending, -ΔR), establishing a nine-command matrix; (D) Logic truth table mapping specific input combinations from Sensors 1 and 2 to nine distinct vehicular motion commands (e.g., forward, reverse, spot turns, and differential steering); (E-H) Real-time photographs (taken by the authors) of the "virtual car racing" demonstration, where the operator controls the vehicle using distinct finger bending modes: (E) idle state (0, 0) for stopping; (F) single-channel actuation (0, -1) for simple steering; (G) mixed-mode actuation (1, -1) for complex differential maneuvers; and (H) dual-channel synchronous actuation (1, 1) for straight acceleration. HMI: Human-machine interface.

In addition to its use in terrestrial HMIs, the combined superhydrophobicity and bidirectional sensitivity of the sensor permit its application in intelligent underwater robotic systems. In hazardous or labor-intensive scenarios such as hull inspection, pipeline maintenance, and underwater surveying, the sensor may function as a robotic "aquatic phantom" (i.e., an automated diver equivalent) to replace human operators [Figure 6A]. While visual cameras are often impeded by turbid waters, our tactile sensor provides reliable nonvisual perception. When the sensor physically encounters an underwater obstacle, its bidirectional response enables the immediate inference of the relative position of the object, providing actionable spatial information for robotic navigation. Mechanistically, the sensor translates the frictional shear force resulting from a collision into specific bending deformations. As illustrated in Figure 6B, a frontal impact (or moving forward into an object) drags the sensor surface backward, inducing outward bending; conversely, a rear impact (or reversing into an object) pushes the surface forward, inducing an inward bending. To experimentally simulate this reconnaissance scenario, a programmable engraving machine was employed to precisely control the lateral movement of the sensor relative to a fixed obstacle [Figure 6C]. Figure 6D depicts a complete scanning cycle where the sensor traverses from right to left and then returns to its initial position. In the noncontact phase, the interface displays a "SAFE" status [Figure 6E]. As the sensor moves leftward and grazes the object, the induced outward bending triggers a sharp positive peak; accordingly, the GUI switches to a "WARNING" state and dynamically plots the signal, reflecting the process of contacting the target from right to left [Figure 6F]. Upon disengagement, the system reverts to "SAFE" [Figure 6G]. Conversely, during the return path

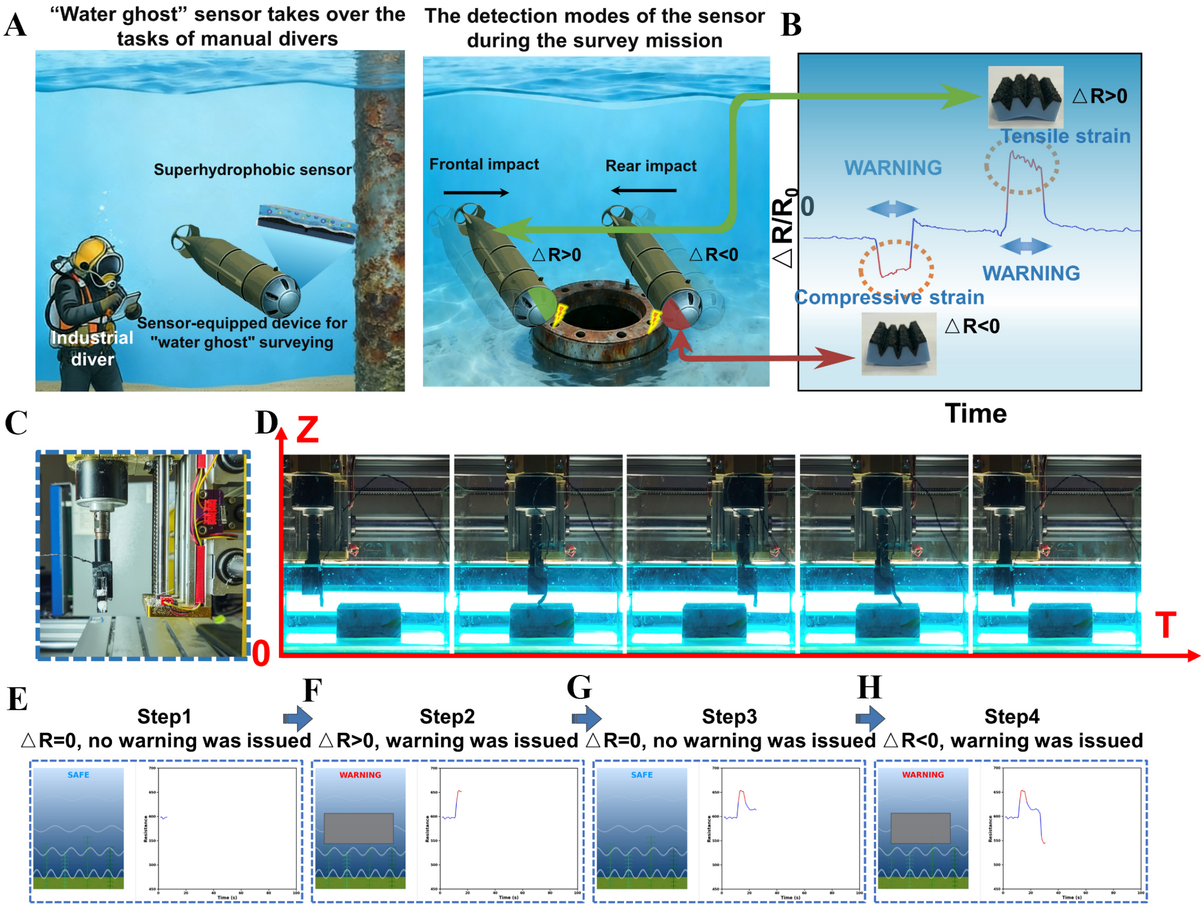

Figure 6. Application of the superhydrophobic sensor as a "aquatic phantom" for intelligent underwater reconnaissance. (A) Schematic of the sensor functioning as a "aquatic phantom" to replace divers. The signal polarity encodes the contact direction as frontal impact induces tension ($\Delta R > 0$) while rear impact induces compression ($\Delta R < 0$); (B) Real-time waveform recording where distinct positive and negative peaks correspond to specific directional collisions; (C and D) Experimental simulation using a programmable engraving machine to precisely control sensor movement, visualized via time-lapse photography along the time axis. The images in (C) and (D) were photographed by the authors; (E-H) real-time demonstration of the sensing process using a Python-based GUI: (e, g) "SAFE" status displayed during noncontact intervals; (F) warning triggered by a negative response ($\Delta R > 0$), indicating outward bending contact; and (H) warning triggered by a positive response ($\Delta R < 0$), indicating inward bending contact. GUI: Graphical user interface.

(rightward movement), the inward bending contact induces a distinct negative dip, prompting the interface to report a "WARNING" signal via the process of contacting the target from left to right [Figure 6H]. This demonstration highlights the unique ability of the sensor to simultaneously detect contact events and resolve spatial directionality in underwater environments, underscoring its promise for constructing intelligent, environment-adaptive robotic skins for autonomous underwater exploration [Supplementary Video 9].

LIMITATIONS

Although the developed slit-based strain sensor achieves high sensitivity and robust superhydrophobicity, it has several limitations. First, while the device exhibits excellent underwater stability in static aquatic settings, the robustness of its electromechanical performance under real-world marine engineering conditions, specifically considering high hydrostatic pressures and dynamic fluid flows, requires further validation. Second, the current manual fabrication process used to achieve the precise microslits may hinder large-scale, high-throughput production. To address these challenges, future work will focus on employing laser-direct writing technologies to enhance structural reproducibility. Additionally, the structural monism design will be optimized to withstand complex hydrostatic and hydrodynamic perturbations, further extending the operational lifespan of the sensor for extreme underwater exploration applications.

CONCLUSIONS

We developed a monolithic, bioinspired superhydrophobic sensor that fundamentally resolves the longstanding conflict between environmental isolation and high-fidelity contact sensing. Inspired by the synergistic survival strategy of the fishing spider, we proposed the concept of structural monism and employed a facile microengraving and solvent-assisted swelling strategy to create an encapsulation-free architecture in which the superhydrophobic layer and sensing element are integrated into a single functional unit. This monolithic architecture endows the sensor with exceptional mechanical flexibility and bidirectional mechanotransduction, enabling the realization of a wearable device for the high-fidelity monitoring of complex joint kinematics in both terrestrial and aquatic settings. Beyond wearable applications, the sensor realizes ternary logic in amphibious settings by resolving the conflict between encapsulation and sensitivity. Its application as a "aquatic phantom" robotic skin demonstrates directional collision perception for underwater spatial mapping, providing a safer, autonomous alternative to human divers for hazardous aquatic reconnaissance.

DECLARATIONS

Authors' contribution

Methodology, formal analysis, investigation, data curation, visualization, and writing - original draft: Wang, Y.; Xu, Y.; Dai, Z.
Conceptualization, supervision, project administration, writing - review and editing: Wang, M.
Supervision, writing - review and editing: Dai, Z.; Xu, W.; Zhang, Q.; Liu, Y.; Qian, K.
Project administration, funding acquisition: Dai, Z.; Qian, K.

Availability of data and materials

The original contributions presented in this study are included in the article/Supplementary Materials. Further inquiries can be directed to the corresponding author(s).

AI and AI-assisted tools statement

Not applicable.

Financial support and sponsorship

This work was supported by the National Natural Science Foundation of China (Grant No. 62401343), the Shandong Provincial Natural Science Foundation (Grant No. ZR2024QF061), and the Guangdong Provincial Natural Science Foundation (Grant No. 2025A1515012947).

Conflicts of interest

All authors declared that there are no conflicts of interest.

Ethical approval and consent to participate

The wearable and underwater demonstrations were performed by a research volunteer under strict safety protocols, with informed consent obtained prior to the study. Tests with volunteers were conducted in compliance with ethical regulations under a protocol approved by the Scientific Research Ethics Committee of School of Integrated Circuits of Shandong University (approval number KJLL-2024-01-006).

Consent for publication

Not applicable.

Copyright

Supplementary Materials

Supplementary Materials

REFERENCES

1. Li, Y.; Schreiber, S.; Yang, H.; et al. From molecules to machines: a multiscale roadmap to intelligent, multifunctional soft robotics. *Chem. Rev*. **2025**, *125*, 8123-245. DOI
2. Ding, S.; Dai, Z.; Zhao, D.; et al. Self-Elevated 3D helical oscillator with addressable eigenfrequency for wearable interface. *Adv. Mater*. **2025**, *38*, e16218. DOI
3. Cao, Y.; Peng, Y.; Ren, W.; et al. Intrinsically soft and fully recyclable robotic sensors with quadruple sensing functions for reliable human-robot interactions. *Science. Bulletin*. **2025**, *70*, 2784-96. DOI
4. Zhu, J.; Sun, B.; Xi, M.; Zhan, Y.; Zhang, B.; Zhu, Y. Flexible electronics in humanoid five senses for the era of artificial intelligence of things (AIoT). *Mater. Today*. **2025**, *88*, 1066-86. DOI
5. Jeon, S. H.; Hwang, G. W.; Kim, J.; et al. Super-adaptive electroactive programmable adhesive materials to challenging surfaces: from intelligent soft robotics to XR haptic interfaces. *InfoMat* **2024**, *7*, e12640. DOI
6. Cao, Y.; Xu, B.; Li, B.; Fu, H. Advanced design of soft robots with artificial intelligence. *Nano-Micro. Lett*. **2024**, *16*, 214. DOI PubMed PMC
7. Baines, R.; Shah, D.; Marvel, J.; Case, J.; Spielberg, A. The need for reproducible research in soft robotics. *Nat. Mach. Intell*. **2024**, *6*, 740-1. DOI
8. Sun, J.; Zhang, C.; Yang, C.; et al. Human skin-inspired neuromorphic sensors. *Soft. Sci*. **2025**, *5*, 18. DOI
9. Yu, S.; Ji, Z.; Liu, L.; et al. A hyperconformal dual-modal metaskin for well-defined and high-precision contextual interactions. *Nat. Commun*. **2025**, *16*, 10573. DOI PubMed PMC
10. Zhao, Q.; Wang, H.; Ni, Z.; et al. Organic nonvolatile 2T memory cell employing a not-gate-like architecture toward binary output level with enhanced noise tolerance. *Adv. Mater*. **2024**, *36*, 2412255. DOI
11. Kong, L.; Fang, Z.; Zhang, T.; et al. A self-powered and self-sensing lower-limb system for smart healthcare. *Adv. Energy. Mater*. **2023**, *13*, 2301254. DOI
12. Yao, K.; Zhuang, Q. Self-decoupling three-axis forces in a simple sensor. *Nat. Mach. Intell*. **2024**, *6*, 1431-2. DOI
13. Wu, T.; Li, Y. T.; Zhao, L.; et al. Recent progress on flexible multimodal sensors: decoupling strategies, fabrication and applications. *Adv. Mater*. **2026**, *38*, e21375. DOI PubMed PMC
14. Sun, Y.; Li, D.; Yang, R.; et al. The Touch-Code Glove: a multimodal mapping interface with triboelectric-digital encoding for intuitive robot training. *Soft. Sci*. **2025**, *5*. DOI
15. Zhang, T.; Qi, H.; Liao, Z.; et al. Engineering crystalline quasi-two-dimensional polyaniline thin film with enhanced electrical and chemiresistive sensing performances. *Nat. Commun*. **2019**, *10*, 4225. DOI PubMed PMC
16. Zhou, W.; Du, Y.; Chen, Y.; et al. Bioinspired ultrasensitive flexible strain sensors for real-time wireless detection of liquid leakage. *Nano-Micro. Lett*. **2024**, *17*, 68. DOI PubMed PMC
17. Kang, D.; Pikhitsa, P. V.; Choi, Y. W.; et al. Ultrasensitive mechanical crack-based sensor inspired by the spider sensory system. *Nature* **2014**, *516*, 222-6. DOI
18. Kim, T.; Hong, I.; Roh, Y.; et al. Spider-inspired tunable mechanosensor for biomedical applications. *npj. Flex. Electron*. **2023**, *7*, 12. DOI
19. Wang, J.; Liu, L.; Yang, C.; et al. Ultrasensitive, highly stable, and flexible strain sensor inspired by nature. *ACS. Appl. Mater. Interfaces*. **2022**, *14*, 16885-93. DOI
20. Wang, Q.; Yao, Z.; Zhang, C.; et al. A selective-response hypersensitive bio-inspired strain sensor enabled by hysteresis effect and parallel through-slits structures. *Nano-Micro. Lett*. **2023**, *16*, 26. DOI PubMed PMC
21. Yu, R.; Wang, C.; Du, X.; et al. *In-situ* forming ultra-mechanically sensitive materials for high-sensitivity stretchable fiber strain sensors. *Natl. Sci. Rev*. **2024**, *11*, nwae158. DOI
22. Lin, H.; Peng, Y.; Zhang, F.; et al. Sandwich-structured electrospun polyvinylidene difluoride sensor for structural health monitoring of glass fiber reinforced polymer composites. *Microstructures* **2024**, *4*, 2024053. DOI
23. Dai, Z.; Lei, M.; Ding, S.; et al. Durable superhydrophobic surface in wearable sensors: From nature to application. *Exploration* **2023**, *4*, 20230046. DOI
24. Wang, C.; Ning, Y.; Yue, Y.; et al. Deformation-induced multioptical morphology elastomer constructed from phosphorescent nanospheres for underwater mechanical sensing. *ACS. Nano*. **2025**, *19*, 8357-70. DOI
25. Shankar, E. G.; Paranjape, M. V.; Yu, J. S. Ecoflex-assisted quasi-solid-state flexible hybrid supercapacitors based on binder-free nanoflower-like $Co_xMo_{3-x}S_3$ and Te-infused radish-derived bio-carbon for sensing and healthcare applications. *Adv. Compos. Hybrid. Mater*. **2025**, *8*, 149. DOI
26. Ding, Z.; Li, W.; Wang, W.; et al. Highly sensitive iontronic pressure sensor with side-by-side package based on alveoli and arch structure. *Adv. Sci*. **2024**, *11*, 2309407. DOI
27. Yao, B.; Zhu, Y.; Jin, F.; et al. Stretchable strain sensors based on liquid metal channels with simultaneous significant improvements in linearity and sensitivity. *Adv. Funct. Mater*. **2025**, *36*, e17648. DOI

28. Yao, Z.; Feng, H.; Shang, K.; Deng, X.; Yang, T. Skin-like strain sensors based on multiwalled carbon nanotube/polydimethylsiloxane composite films. *ACS. Appl. Nano. Mater.* **2023**, *6*, 6550-8. DOI
29. Sun, R.; Wu, P.; Li, P.; et al. Enhancing the hydrophobicity of triboelectric sensors with biomimetic structure for motion recognition of field robots. *Chem. Eng. J.* **2025**, *507*, 160600. DOI
30. Kong, H.; Li, W.; Song, Z.; Niu, L. Recent advances in multimodal sensing integration and decoupling strategies for tactile perception. *Mater. Futures.* **2024**, *3*, 022501. DOI
31. Liu, G.; Yang, J.; Zhang, K.; et al. Recent progress on the development of bioinspired surfaces with high aspect ratio microarray structures: from fabrication to applications. *J. Controlled. Release.* **2024**, *367*, 441-69. DOI
32. Kim, M.; Park, H.; Kim, M.; et al. Fluoropolymer-based organic memristor with multifunctionality for flexible neural network system. *npj. Flex. Electron.* **2021**, *5*, 34. DOI
33. Yang, Q.; Li, X.; Xue, Y.; et al. Recent advances in fluorinated superhydrophobic materials: Preparation and diverse applications. *Chem. Eng. J.* **2025**, *523*, 168236. DOI
34. Botas, A. M.; Carvalho, A. F.; Fernandes, A. J.; et al. Laser patterning for fast production of superhydrophobic copper with delayed formation of patina and maintenance of surface electrical conductivity. *Appl. Surf. Sci.* **2025**, *686*, 162108. DOI
35. He, J.; Xue, K.; Liu, Q.; et al. High-sensitivity, superhydrophobic, and flame-retardant wearable flexible sensor for human motion monitoring and underwater signal transmission. *Adv. Mater. Technol.* **2026**, *11*, e02409. DOI
36. Feng, Y.; Zhu, W.; Yang, X.; et al. Amphibian-inspired conductive ionogel stabilizing in air/water as a wearable amphibious flexible sensor for drowning alarms. *Chin. Chem. Lett.* **2025**, *36*, 110554. DOI
37. Li, J.; Tao, J.; Ge, C.; et al. An integrated sensing and communication solar skin for health monitoring and human-machine interaction. *Nano. Energy.* **2026**, *148*, 111639. DOI
38. Yang, Q.; Li, B.; Wang, M.; et al. Machine learning-enhanced modular ionic skin for broad-spectrum multimodal discriminability in bidirectional human-robot interaction. *Adv. Mater.* **2025**, *37*, e08795. DOI
39. Chen, H.; Huang, Z.; Luo, Y.; et al. Bioinspired cross-modal self-adaptive machine intelligence for event-driven and ultrahigh-precision underwater grasping. *Adv. Mater.* **2026**, *38*, e19665. DOI